A Dynamic Photovoltaic Model Incorporating Capacitive and Reverse-Bias Characteristics

Katherine A. Kim, *Student Member, IEEE*, Chenyang Xu, *Student Member, IEEE*, Lei Jin, *Student Member, IEEE*, and Philip T. Krein, *Fellow, IEEE*

Abstract—Photovoltaics (PVs) are typically modeled only for their forward-biased dc characteristics, as in the commonly used single-diode model. While this approach accurately models the *I–V* curve under steady forward bias, it lacks dynamic and reverse-bias characteristics. The dynamic characteristics, primarily parallel capacitance and series inductance, affect operation when a PV cell or string interacts with switching converters or experiences sudden transients. Reverse-bias characteristics are often ignored because PV devices are not intended to operate in the reverse-biased region. However, when partial shading occurs on a string of PVs, the shaded cell can become reverse biased and develop into a hot spot that permanently degrades the cell. To fully examine PV behavior under hot spots and various other faults, reverse-bias characteristics must also be modeled. This study develops a comprehensive mathematical PV model based on circuit components that accounts for forward bias, reverse bias, and dynamic characteristics. Using a series of three experimental tests on an unilluminated PV cell, all required model parameters are determined. The model is implemented in MATLAB Simulink and accurately models the measured data.

Index Terms—Characterization, dynamic model, photovoltaic cells, reverse breakdown, simulation tool.

I. Introduction

ACCURATE photovoltaic (PV) models are needed to simulate PV cells and panels at a detailed level without long computation time. Applications that require these models include the PV emulation equipment used for controllable indoor experiments and large-scale simulations that would otherwise be very costly to build [1]. Appropriate PV models trade-off simplicity with accuracy to run the required calculations quickly, while providing enough detail to model the desired characteristics.

The most common PV model is the single-diode circuit model, which is a nonlinear dc model that is fully detailed in works such as [2], [3]. There are various more detailed PV models described in [4] and [5] that mainly focus on accuracy for dc characteristics in the forward-biased region. The dynamic and reverse-bias characteristics are commonly neglected, but these characteristics do affect PV operation, particularly, in fault conditions and high-frequency applications. This study emphasizes the capacitive, inductive, and reverse-bias characteristics that are incorporated in the proposed PV model.

Dynamic characteristics are apparent when PVs are connected to switch-mode power converters [6] and should not be ignored. PVs exhibit nonlinear parallel capacitance [7] that can be modeled in a similar way to p-n junction diode capacitance, as in [8]–[11]. There are a number of established PV models that include parallel capacitance. In [12], PV cell capacitance is measured using frequency analysis and modeled as diffusion capacitance. In [7], Si cells are tested at different temperatures, and capacitance is modeled as diffusion and junction capacitance. In [13], both capacitive and inductive aspects are modeled and identified using time-domain analysis. In [1], a PV model with inductance and diffusion capacitance is implemented in MATLAB Simulink and Plexim PLECS. While these models capture dynamic characteristics, they do not incorporate reverse-breakdown characteristics.

The reverse-biased characteristics are necessary for accurately emulating a string under mismatch or partial shading conditions, where the shaded cell becomes reverse biased. When PVs are reverse biased past a certain threshold, the p-n junction goes into reverse breakdown, which results in significant reverse current through the cell. This current flow heats the material, creating a hot spot that can degrade or damage the cell [14], [15]. Bypass diodes are commonly placed across PV strings to mitigate hot spot formation, but it does not completely eliminate the problem [16]. Accurately modeling reverse-biased characteristics is necessary to further examine mismatch effects in PV strings. There are some PV models that incorporate reverse breakdown effects, as in [4] and [17], but the model is not compared to measured data and a parameter identification procedure is not provided. Because the literature on modeling PVs in reverse bias is limited, the p-n junction diode literature was also investigated. A detailed p-n junction diode model incorporating tunneling and avalanche effects is described in [18]
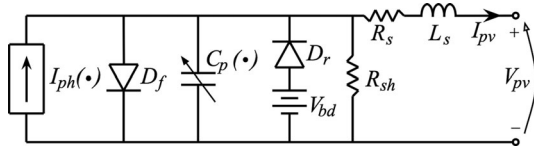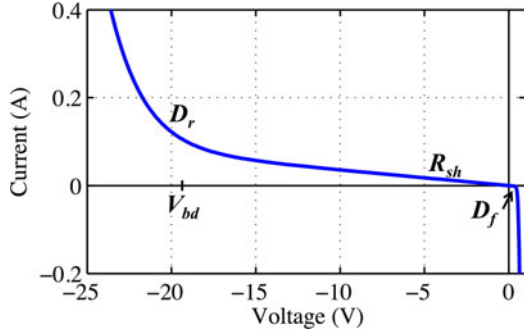
Fig. 1.   Dynamic PV model equivalent circuit.

Fig. 2.   PV *I–V* curve showing where the characteristics of each equivalent circuit component dominate the curve.

and [19], but requires detailed manufacturing and material data that are not publicly available.

While PV forward-bias, dynamic, reverse-breakdown characteristics have been explored at various levels of detail in the previous literature, there is a need for a comprehensive model incorporating all of these aspects. This study describes a dynamic circuit-based PV model for both forward and reverse bias that incorporates parallel capacitance and series inductance. The governing mathematical equations and physical reasoning are provided. Model parameters are identified from both datasheet information and measured data. One dc sweep and two ac frequency sweep tests are conducted to fully define the model parameters. The model is implemented in MATLAB Simulink as a standalone block that is made publicly available.

II. PROPOSED DYNAMIC PHOTOVOLTAIC MODEL

A PV cell is essentially a p-n junction with parasitic resistances, capacitance, and inductance that can be modeled using circuit components, plus a current source representing photocurrent. The full PV equivalent circuit model is shown in Fig. 1. In addition to the basic single-diode PV model, which consists of the photocurrent source $I_{\rm ph}(\cdot)$, forward-bias conduction diode D_f, shunt resistance $R_{\rm sh}$, and series resistance R_s, this model incorporates a series inductance L_s, variable parallel capacitance $C_p(\cdot)$, and reverse-bias conducting diode D_r with a breakdown voltage offset $V_{\rm bd}$. This is the large-signal model for a PV cell. Fig. 2 shows the regions where D_f, $R_{\rm sh}$, and D_r are most prominent in the *I–V* curve. Forward diode D_f characteristics dominate under forward voltage bias. Reverse diode D_r characteristics dominate when reverse-biased beyond the breakdown voltage $V_{\rm bd}$, which emulates avalanche and zener breakdown. In between 0 and $V_{\rm bd}$, where neither diode is conducting significant current, resistive characteristics of $R_{\rm sh}$ dominate. Although not explicitly labeled, R_s characteristics are most prominent past

TABLE I
PV MODEL VARIABLES

Model Input	
G	irradiance [W/m^2]
T	temperature [$^\circ C$]
I_{pv}	PV current [A]
Model Output	
V_{pv}	PV voltage [V]
Internal Parameters	
k	Boltzmann constant [J/K]
q	electron charge [C]
G_n	nominal irradiance [W/m^2]
T_n	nominal temperature [K]
Datasheet Parameters	
I_{scn}	nominal short circuit current [A]
V_{ocn}	nominal open circuit voltage [V]
I_{mpp}	maximum power point current [A]
V_{mpp}	maximum power point voltage [V]
K_i	current temperature coefficient [A/K]
K_v	voltage temperature coefficient [V/K]
N_s	number of cells in series
Measured Parameters	
R_s	series resistance [Ω]
R_{sh}	shunt resistance [Ω]
L_s	series inductance [H]
a	diode ideality factor
V_{bd}	breakdown voltage [V] (negative value)
I_{sr}	reverse saturation current [A]
K_r	reverse breakdown scalar coefficient
C_{j0}	zero-bias junction capacitance [F]
ϕ_0	zero-bias junction potential [V]
τ	mean carrier lifetime [s]
τ_{bd}	breakdown mean carrier lifetime [s]

the "knee" of the diode characteristics, i.e., above the maximum power point (MPP) voltage and below $V_{\rm bd}$.

PV characteristics are affected by changes in illumination G and temperature T. The model is set up such that G, T, and PV current $I_{\rm pv}$ are inputs, and the output is the resulting PV voltage $V_{\rm pv}$. All model variables and units are outlined in Table I. A portion of the parameters are taken from the datasheet; the rest are determined from measured data.

The model assumes passive components R_s, L_s, and $R_{\rm sh}$ are constant—effects of G and T are negligible on them. The R_s and L_s are associated with the physical length, area, and shape of the leads. These values tend to be small for individual cells, but can be substantially higher for PV panels. Larger R_s leads to higher conduction losses, particularly for cells with higher rated current levels. The $R_{\rm sh}$ value is linked to the PV material, thickness, and manufacturing quality. The parallel capacitance C_p value is not constant; it is affected by the PV operating point. Similarly, the forward diode D_f and reverse diode D_r have nonlinear characteristics that are affected by temperature.

A. Governing Equations Development

The proposed PV model governing equations are based on the equivalent circuit model, shown in Fig. 1. First, the parallel components are described relative to the PV model inputs (G, T, $I_{\rm pv}$) and voltage over the forward diode V_d, and V_d is solved for using a nonlinear solving technique. Then, the model output

$V_{\rm pv}$ is determined from V_d and $I_{\rm pv}$ using the series element's governing equations.

1) Photocurrent: The photocurrent $I_{\rm ph}$ represents the current of electrons excited by illumination. Its value is directly proportional to G, with the difference between T and nominal temperature T_n creating a small offset. The governing equation for $I_{\rm ph}$ is

$$I_{\rm ph}(G,T) = \left[I_{\rm scn}\left(\frac{R_s + R_{\rm sh}}{R_{\rm sh}} \right) + K_i(T - T_n) \right] \frac{G}{G_n} \quad (1)$$

where $I_{\rm scn}$ is the nominal short-circuit current, K_i is the current temperature coefficient, and G_n is the nominal irradiance [2].

2) Diodes: Both forward and reverse diodes are affected by temperature T through the thermal voltage

$$V_t(T) = \frac{kT}{q} N_s \quad (2)$$

where k is Boltzmann's constant, q is an electron charge, and N_s is the number of series cells. The forward diode D_f conducts when the PV is forward biased, and its current I_{df} is

$$I_{df}(T, V_d) = I_s(T)\left[\exp\left(\frac{V_d}{aV_t(T)} \right) - 1 \right] \quad (3)$$

where a is the diode ideality factor that ranges from 1 to 2 and the diode saturation current I_s, as derived in [2], is

$$I_s(T) = \frac{I_{\rm scn} + K_i(T - T_n)}{\exp\left(\frac{V_{\rm ocn} + K_v(T - T_n)}{aV_t(T)} \right) - 1} \quad (4)$$

where $V_{\rm ocn}$ is the nominal open-circuit voltage, and K_v is the voltage temperature coefficient. The reverse diode D_r conducts current when the PV is reverse biased, and its current I_{dr} is

$$I_{dr}(T, V_d) = I_{sr}\exp\left(\frac{K_r V_{\rm bd}}{aV_t(T)} \right)\left[\exp\left(\frac{-K_r V_d}{aV_t(T)} \right) - 1 \right]. \quad (5)$$

Note that current is defined in D_r's forward-conducting direction and $V_{\rm bd}$ is a negative voltage. Even between cells with similar forward characteristics, reverse characteristics can vary widely [19]. The aim of this model is to capture general reverse-breakdown trends without delving into intricate nonidealities.

3) Parallel Capacitor: PV parallel capacitance C_p comes from the sum of three different sources: junction, diffusion, and breakdown capacitance. These capacitances are nonlinear values that depend on temperature and the operating point. Fig. 3 shows C_p as a function of $V_{\rm pv}$ and the regions where each type of capacitance dominates.

Junction or transition capacitance C_j comes from charge stored in the depletion region at the semiconductor p-n junction. It dominates at small positive and negative voltages, where the junction is not conducting significant current [8]–[10]. The C_j is determined according to

$$C_j(V_d) = \frac{C_{j0}}{\sqrt{1 - \frac{V_d}{N_s \phi_0}}} \quad (6)$$

as done in [11], where C_{j0} is the zero-voltage capacitance, and ϕ_0 is the zero-voltage junction potential. The ϕ_0 is an upper
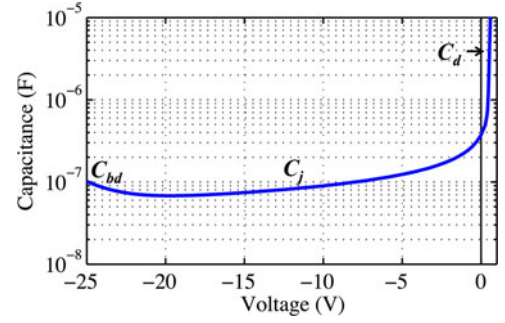

Fig. 3. Parallel capacitance over PV voltage showing where breakdown ($C_{\rm bd}$), junction (C_j), and diffusion (C_d) capacitance dominate.

voltage bound for the model; therefore, it should hold that $\phi_0 > V_{\rm ocn}$.

Diffusion capacitance C_d comes from the charge stored in the neutral region of the semiconductor outside the depletion region. Thus, it dominates above the MPP voltage, where the junction carries significant current. The magnitude of C_d tends to be larger than that of C_j. It is prominent when the p-n junction is forward biased and negligible when reverse biased. The C_d is directly proportional to the diode junction current I_{df} according to

$$C_d(T, V_d) = \frac{\tau I_{df}(T, V_d)}{aV_t(T)} \quad (7)$$

where τ is mean carrier lifetime [8].

Breakdown capacitance $C_{\rm bd}$ dominates when the cell goes into reverse breakdown. Tunneling, Shockley–Read–Hall recombination, and avalanche are physical factors that contribute to p-n junction breakdown [19]; modeling these factors individually would result in an overly complicated model. In an effort to maintain simplicity, $C_{\rm bd}$ is modeled similarly to C_d such that

$$C_{\rm bd}(T, V_d) = \frac{\tau_{\rm bd} I_{dr}(T, V_d)}{aV_t(T)} \quad (8)$$

where $\tau_{\rm bd}$ is the effective carrier lifetime under breakdown.

The overall parallel capacitance C_p is

$$C_p(T, V_d) = C_j(V_d) + C_d(T, V_d) + C_{\rm bd}(T, V_d) \quad (9)$$

where C_j, C_d, and $C_{\rm bd}$ must be positive; if any capacitance result is negative, it is set to 0. Parallel capacitance current I_{Cp} is governed by

$$I_{Cp}(V_d) = C_p(T, V_d)\frac{dV_d}{dt} \quad (10)$$

4) Shunt Resistance: Shunt resistor current $I_{R\rm sh}$ is

$$I_{R\rm sh}(V_d) = \frac{V_d}{R_{\rm sh}} \quad (11)$$

according to Ohm's law.

5) Diode Voltage: Applying Kirchhoff's current law to these currents yields

$$0 = I_{\rm ph}(G,T) - I_{df}(T, V_d) - I_{Cp}(V_d)$$
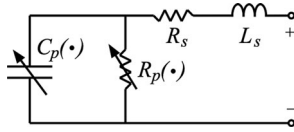$$+ I_{dr}(T, V_d) - I_{R\rm sh}(V_d) - I_{\rm pv} \quad (12)$$

Fig. 4. Ac small-signal PV model, where R_s and L_s are static, and $C_p(\cdot)$ and $R_p(\cdot)$ depend upon environmental and operating conditions.

which is a nonlinear equation that can be solved for V_d given G, T, and I_{pv} as inputs. Nonlinear problem solving techniques, such as Newton–Raphson, can be employed. The differential term I_{Cp} can be solved for with standard numerical integration techniques used for simulation.

6) PV Voltage: Once the diode voltage V_d is determined, PV voltage V_{pv} is calculated according to

$$V_{\mathrm{pv}}(V_d, I_{\mathrm{pv}}) = V_d - I_{\mathrm{pv}} R_s - L_s \frac{dI_{\mathrm{pv}}}{dt}. \tag{13}$$

The differential term here is also solved for using numerical integration simulation techniques.

B. Alternate Current Small-Signal Model

The small-signal model is analyzed for completeness and also to calculate the capacitance C_p and inductance L_s values. The ac small-signal model is depicted in Fig. 4. Under ac analysis the R_s, L_s, and $C_p(\cdot)$ values are equivalent to the previously described large-signal model. The I_{ph}, diode characteristics for D_f and D_r, and R_{sh} become an equivalent parallel resistance $R_p(\cdot)$, whose impedance depends on G, T, I_{pv}, and V_d. Small-signal impedance Z is expressed mathematically as

$$Z = \left[R_s + \frac{R_p}{\alpha + 1} \right] + j \left[L_s \omega - \frac{\omega R_p^2 C_p}{\alpha + 1} \right] \tag{14}$$

where $\omega = 2\pi f$ is the radian frequency, and $\alpha = \omega^2 R_p^2 C_p^2$.

III. EXPERIMENTAL TESTS

Basic datasheet information and three experimental tests are used to identify all required model parameters. All tests are conducted on unilluminated (dark) PV cells, such that these tests can be conducted in a typical electronics lab without expensive solar simulator equipment. A Keithley 2429 SourceMeter was used as a dc power source, an Agilent 33250A Function Generator with a transformer generated the ac signal, a Textronix MSO4034 Oscilloscope captured and recorded the ac waveforms, and a computer running a Python script that communicates via GPIB automated the process.

A. Datasheet Information

PV datasheets typically supply nominal operating characteristics such as the short-circuit current I_{scn}, open-circuit voltage V_{ocn}, MPP voltage V_{mpp}, and MPP current I_{mpp}. Most datasheets also supply a V_{oc} temperature coefficient K_v and an I_{sc} temperature coefficient K_i. If the temperature coefficient is not supplied, the value can be estimated based on PV modules of
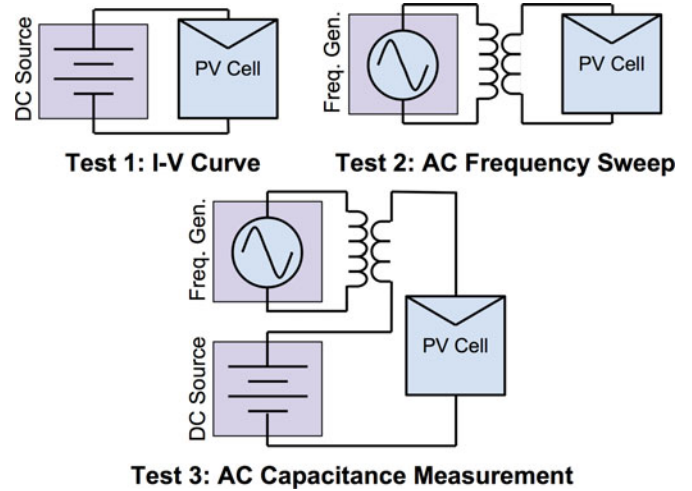

Fig. 5. Equipment setup for the three PV characterization tests.

the same material, e.g., $K_v = 176.6$ mV/K and $K_i = 3.5$ mA/K for monocrystalline Si Sunpower cells [20].

B. Test 1: Current–Voltage Curve

The first test measures the *I–V* curve, where the power source is directly connected to the PV under test, as illustrated in Fig. 5. The measurement range must be wide enough and at a high enough resolution to accurately capture both forward diode and the reverse-breakdown characteristics. For Test 1, the power source was set in constant-current mode and swept over the operating range in 1 mA increments.

C. Test 2: Alternate Current Frequency Sweep

The second test is an ac frequency sweep on the unilluminated PV cell under no dc bias (0 V, 0 A) to identify R_s and L_s. The function generator connects through a transformer (for isolation) to the PV, as shown in Fig. 5. The following component value calculations are based on magnitude measurements only and not on the phase angle; if desired, values could also be derived based on phase angle measurements.

Fig. 6 shows an example bode plot for the ac small-signal PV model described in (14). The lowest impedance value is the resonance point, which is equivalent to R_s. The lowest measured impedance from the ac frequency sweep is taken as R_s. Then, R_p is calculated from a low-frequency impedance measurement $Z_{\mathrm{low}f}$ according to

$$R_p = |Z_{\mathrm{low}f}| - R_s. \tag{15}$$

In the mid-frequency range, the impedance magnitude begins to decrease with increasing frequency because C_p characteristics dominate. From this mid-frequency impedance magnitude $|Z_{\mathrm{mid}f}|$, C_p is

$$C_p = \frac{1}{R_p \omega} \sqrt{\frac{(R_s + R_p)^2 - |Z_{\mathrm{mid}f}|^2}{|Z_{\mathrm{mid}f}|^2 - R_s^2}} \tag{16}$$

assuming R_s and R_p were already determined. Above the resonant point, L_s dominates and impedance magnitude increases
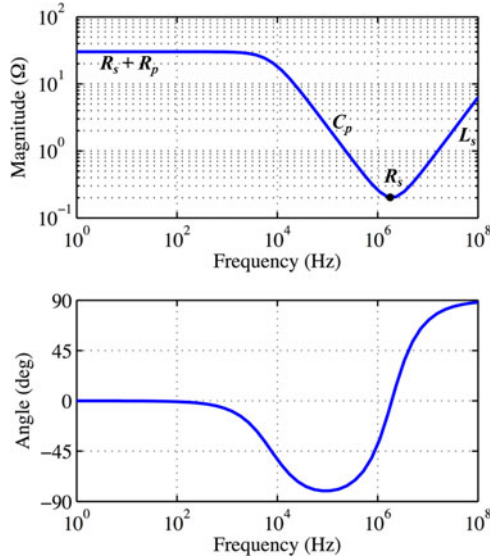
Fig. 6.   PV ac small-signal model bode plot.

with frequency. In this high-frequency range, impedance magnitude $|Z_{\mathrm{high}f}|$ is used to calculate L_s according to

$$L_s = \frac{1}{\omega}\sqrt{|Z_{\mathrm{high}f}|^2 - \frac{R_s + R_p}{1+\alpha} + \frac{R_p^2 C_p}{1+\alpha}} \qquad (17)$$

using the known R_s, R_p, and C_p values.

As frequency increases beyond 1 MHz, parasitics or unintentional coupling from cables and connectors are more likely to affect the measurement. The frequency needed to calculate L_s must be higher than the resonant point, but choosing a frequency on the lower end of this range is advisable. In this paper, measurements at 2 MHz were used to calculate L_s. Also, using shorter cables and connectors with short leads can reduce inductance loops and reduce the measurement error.

D. Test 3: Alternate Current Measurements for Capacitance

The third test is a constant-frequency ac measurement to determine C_p at various operating points. The power source is in series with the transformer driven by the function generator such that the ac measurement can be taken over a range of dc operating points, as shown in Fig. 5. At each operating point, first R_p is calculated at 500 Hz according to (15) and C_p is calculated at 100 kHz according to (16). Breakdown voltage V_{bd} is chosen as the voltage with the lowest measured capacitance.

IV. PARAMETER FITTING

A monocrystalline (m-c) and a poly-crystalline (p-c) Si PV cell of the same dimension (6 in. × 6 in.) were subjected to the three tests described in Section III. The R_s and L_s were identified from Test 2, and V_{bd} from Test 3. The remaining parameters were found using the MATLAB Curve Fitting Toolbox *fit* function employing a nonlinear least-squares method to fit parameter values to the measured data. For each parameter (or pair of parameters), the associated governing equation is specified
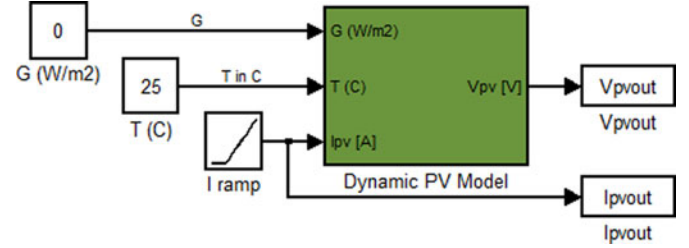

Fig. 7.   PV model implemented as a Simulink block.

using the *fittype* function and the best-fit parameter values are identified.

From the *I–V* curve measured in Test 1, R_{sh} is determined as the linear fit of the curve from $V_{\mathrm{bd}}/2$ to $V_{\mathrm{mpp}}/2$, where the *I–V* curve is relatively linear. The current through R_{sh} is subtracted according to (11), and the voltage over R_s is subtracted according to Ohm's law. The resulting *I–V* curve, with parasitic resistances calculated out, only exhibits characteristics for the forward and reverse diodes; it is used to fit (3) in the forward-bias region to determine a and (5) in the reverse-bias region to determine I_{sr} and K_r.

Next, the capacitance–voltage (*C–V*) curve, measured in Test 3, is split into three regions: below V_{bd}, between V_{bd} and V_{mpp}, and above V_{mpp}, which correspond to breakdown, junction, and diffusion capacitance, respectively. First, the transition capacitance is fit to *C—V* curve from V_{bd} to V_{mpp} according to (6) to determine C_{j0} and ϕ_0. The transition capacitance is subtracted from the measured capacitance such that the resulting *C–V* curve represents diffusion and breakdown capacitance. Then, the diffusion capacitance is fit in the forward region above V_{mpp} according to (7) to determine τ, and breakdown capacitance is fit in the breakdown region below V_{bd} according to (8) to determine τ_{bd}.
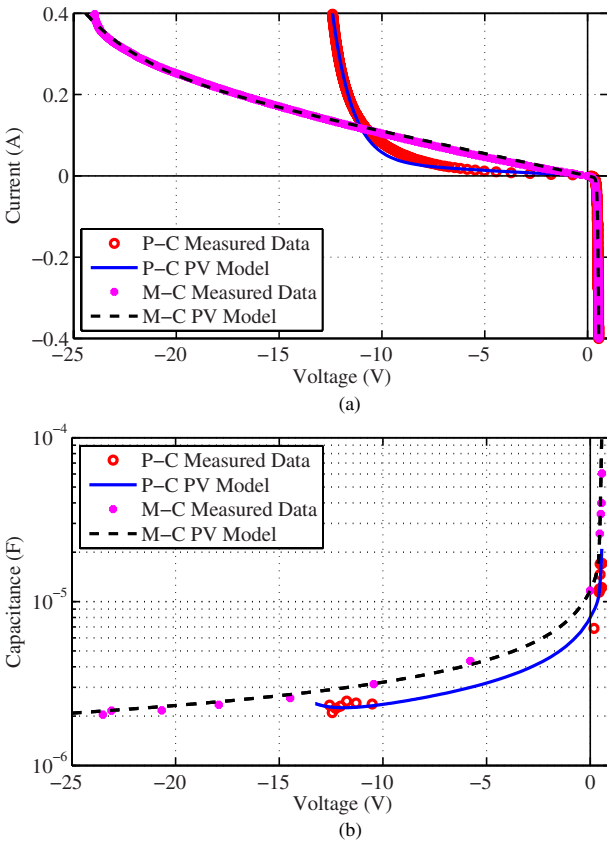
The full dynamic PV model is implemented in MATLAB Simulink blocks; an *algebraic constraint* block is used to solve (12). The PV model is implemented as a stand-alone block, shown in Fig. 7, that masks the numerous equations and allows users who are less familiar with PV modeling to utilize the block as a tool. Simulink models for both cells are publicly available at http://katherinekim.net/PVmodel.html. The Python code used to run the three tests and parameter fitting MATLAB code is also available for download.

A. Polycrystalline Si Cell

The measured p-c cell was an unused grade BB2 cell; its full parameter set is summarized in Table II. The cell's *I–V* curve for the measured data and model are compared in Fig. 8(a). The model fits well to the data over the full range of operation, with only a slight divergence around the breakdown voltage. The cell has a high R_{sh} and low V_{bd}, which means the cell exhibits good reverse-blocking characteristics. The p-c cell's measured and modeled *C–V* curves are compared in Fig. 8(b). Below $V_{\mathrm{bd}} = -12.0$ V, capacitance begins to increase due to breakdown capacitance, which is neglected in most PV models,

TABLE II
PV MODEL PARAMETERS FOR P-C AND M-C SI CELLS

parameter	p-c cell	m-c cell	unit
k	$1.3806503 \times 10^{-23}$		J/K
q	$1.60217646 \times 10^{-19}$		C
G_n	1000		W/m^2
T_n	298.15		K
I_{scn}	8.49	7.61	A
V_{ocn}	0.623	0.624	V
I_{mpp}	7.89	7.03	A
V_{mpp}	0.46	0.45	V
K_i	0.00552	0.00495	A/K
K_v	-0.00224	-0.00224	V/K
N_s	1	1	
R_s	0.070	0.0460	Ω
R_{sh}	371	91.8	Ω
L_s	7.94×10^{-8}	5.00×10^{-8}	H
a	1.38	1.31	
V_{bd}	-12.0	-23.5	V
I_{sr}	0.246	0.0997	A
K_r	0.0369	0.0114	
C_{j0}	7.95×10^{-6}	1.17×10^{-5}	F
ϕ_0	0.956	0.82	V
τ	6.50×10^{-7}	5.76×10^{-6}	s
τ_{bd}	1.32×10^{-8}	0	s

Fig. 9. (a) *I–V* and (b) *C–V* curves comparing measured data and model for the p–c PV cell under dark and illuminated conditions. (a) Current versus voltage. (b) Capacitance versus voltage.

B. Monocrystalline Si Cell

The measured m-c Si cell was an unused grade BB3 cell (one grade below the p-c cell); its parameters are also summarized in Table II. Fig. 8(a) compares the measured and modeled *I–V* curves. This cell shows a lower $R_{\rm sh}$ (attributed to the lower grade) and lower $V_{\rm bd}$ (attributed to more uniform crystalline structure) than the p-c cell. The model fits well to the data over the operating range with only a slight divergence below $V_{\rm bd}$. The measured range was limited thermally, i.e., imposing higher currents heated up the cell, altering the *I–V* characteristics. Accurate measurements over a larger range would result in better fit parameters, but the parameters are adequate for the given operating range. Fig. 8(b) shows the m-c measured and modeled *C–V* curves, which are well matched. While the transition and diffusion capacitance trends are clear, voltage does not become sufficiently reverse biased to observe breakdown capacitance trends. Breakdown capacitance can be easily ignored in this cell by setting $\tau_{\rm bd} = 0$.

Fig. 8. (a) *I–V* and (b) *C–V* curves comparing measured data and model for the p-c and m-c PV cell. (a) Current versus voltage. (b) Capacitance versus voltage.

but is apparent in this cell. The proposed model shows good fitting in all three capacitive regions.

V. ILLUMINATION EXPERIMENT

The p-c cell is tested under an indoor illumination setup using a halogen light powered by a dc supply so that the 60 Hz grid frequency did not interfere with the ac tests. The cell was

illuminated at 60 W/m^2—a relatively low irradiance to reduce temperature increase—and Tests 1 and 3 were performed on the cell. The p-c cell model was simulated under the same conditions. Fig. 9 compares the dark and illuminated results. Fig. 9(a) shows the I–V curve; except for some deviation around the breakdown voltage, general characteristics exhibits good matching between model and data. Fig. 9(a) shows the C–V curve in the forward-biased region, where the illumination increases diffusion capacitance. The measured data appears to have a slightly higher increase than predicted by the model, but the general trends are consistent. Illumination had little effect on the capacitance in the reverse-biased region. Further improvements to this model might focus on better fitting the reverse-biased and capacitive characteristics to changes in illumination and temperature, which is left as future work.

VI. Conclusion

A mathematic PV model with nonlinear dynamic characteristics in both forward- and reverse-bias regions is developed and fully described in (1)–(13). The model incorporates reverse breakdown, series inductance, and transition, diffusion, and breakdown capacitance that are not commonly modeled. A set of three tests conducted with basic electronics equipment along with basic fitting tools in MATLAB are used to identify all model parameters for a measured PV cell. The model is fit to both a p-c and m-c Si cell, and show good matching for both I–V and C–V curves over the desired range. If breakdown capacitance is not observed over the measured range, it can be omitted without fundamentally changing the model. Under illumination, the I–V curve is well matched and the C–V curve follows accurate trends. This detailed dynamic model is effective for emulating faults, hot spots, and interactions with switching converters.

References

[1] M. C. D. Piazza and G. Vitale, *Photovoltaic Sources: Modeling and Emulation*. London, U.K.: Springer-Verlag, 2013.
[2] M. G. Villalva, J. R. Gazoli, and E. Filho, "Comprehensive approach to modeling and simulation of photovoltaic arrays," *IEEE Trans. Power Electron.*, vol. 24, no. 5, pp. 1198–1208, May 2009.
[3] S. R. Wenham, M. A. Green, M. E. Watt, and R. Corkish, *Appl. Photovoltaics*. London, U.K.: Earthscan, 2008.
[4] A. Izadian, A. Pourtaherian, and S. Motahari, "Basic model and governing equation of solar cells used in power and control applications," in *Proc. IEEE Energy Convers. Congr. Expo.*, Sep. 2012, pp. 1483–1488.
[5] A. Ortiz-Conde, D. Lugo-Munoz, and F. J. Garcia-Sanchez, "An explicit multiexponential model as an alternative to traditional solar cell models with series and shunt resistances," *IEEE J. Photovolt.*, vol. 2, no. 3, pp. 261–268, Jul. 2012.
[6] N. Benavides and P. Chapman, "Modeling the effect of voltage ripple on the power output of photovoltaic modules," *IEEE Trans. Ind. Electron.*, vol. 55, no. 7, pp. 2638–2643, Jul. 2008.
[7] R. A. Kumar, M. S. Suresh, and J. Nagaraju, "Silicon (BSFR) solar cell ac parameters at different temperatures," *Sol. Energy Mater. Sol. Cells*, vol. 85, no. 3, pp. 397–406, Jan. 2005.
[8] J. Millman and C. C. Halkias, *Integrated Electronics*. New York, NY, USA: McGraw-Hill, 1972.
[9] R. King, *Electronics Circuits and Systems*. New York, NY, USA: Wiley, 1975.
[10] R. F. Pierret, *Semiconductor Device Fundamentals*. New York, NY, USA: Addison-Wesley, 1996.
[11] L. T. Pillage, R. A. Rohrer, and C. Visweswariah, *Electronic Circuit and System Simulation Methods*. New York, NY, USA: McGraw-Hill, 1998.
[12] G. J. Madden and A. Le, "Solar panel model for design and analysis of power regulation equipment," in *Proc. Intersoc. Energy Convers. Eng. Conf.*, Aug. 1994, pp. 151–156.
[13] M. C. Di Piazza, M. Luna, and G. Vitale, "Dynamic PV model parameter identification by least-squares regression," *IEEE J. Photovolt.*, vol. 3, no. 2, pp. 799–806, Apr. 2013.
[14] M. Alonso-Garcia, J. Ruiz, and F. Chenlo, "Experimental study of mismatch and shading effects in the I–V characteristic of a photovoltaic module," *Sol. Energy Mater. Sol. Cells*, vol. 90, no. 3, pp. 329–340, Feb. 2006.
[15] S. Spanoche, J. Stewart, S. Hawley, and I. Opris, "Model-based method for partially shaded pv module hot-spot suppression," *IEEE J. Photovolt.*, vol. 3, no. 2, pp. 785–790, Apr. 2013.
[16] Q. Zhang and Q. Li, "Temperature and reverse voltage across a partially shaded Si PV cell under hot spot test condition," in *Proc. IEEE Photovolt. Spec. Conf.*, Jun. 2012, pp. 1344–1347.
[17] D. Giaffreda, M. Omana, D. Rossi, and C. Metra, "Model for thermal behavior of shaded photovoltaic cells under hot-spot condition," in *Proc. IEEE Int. Symp. Defect Fault Tolerance VLSI Nanotechnol. Syst.*, 2011, pp. 252–258.
[18] Y. Subramanian and R. B. Darling, "Compact modeling of avalanche breakdown in pn-junctions for computer-aided ESD design (CAD for ESD)," in *Proc. Int. Conf. Model. Simulat. Microsyst.*, Mar. 2001, pp. 48–51.
[19] G. A. M. Hurkx, H. C. de Graaff, W. J. Kloosterman, and M. P. G. Knuvers, "A new analytical diode model including tunneling and avalanche breakdown," *IEEE Trans. Electron Devices*, vol. 39, no. 9, pp. 2090–2098, Sep. 1992.
[20] "Sunpower E20/327 solar panel," Datasheet, Sunpower, San Jose, CA, USA, 2012

Katherine A. Kim (S'06) received the B.S. degree in electrical and computer engineering from the Franklin W. Olin College of Engineering, Needham, MA, USA, in 2007. She received the M.S. degree in electrical and computer engineering from the University of Illinois at Urbana-Champaign, Urbana, IL, USA, in 2011, where she is currently working toward the Ph.D. degree.

Her current research interests include power electronics, modeling, control, and protection for photovoltaic systems.

Ms. Kim received the National Science Foundation's East Asia and Pacific Summer Institutes Fellowship in 2010 and Graduate Research Fellowship in 2011. She is the Student Membership Chair for the IEEE Power Electronics Society. She served as the Chair of the IEEE Power and Energy Society/Power Electronics Society Joint Student Chapter at the University of Illinois in 2010–2011 and as the Co-Director of the IEEE Power and Energy Conference at Illinois in 2012.

Chenyang Xu (S'11) was born in Taiyuan, China, in 1990. He is currently working toward the B.S. degree in electrical engineering with the University of Illinois at Urbana-Champaign, Urbana, IL, USA.

Since March 2011, he has been an Undergraduate Researcher with the Department of Electrical and Computer Engineering, studying power electronics and its applications. In 2013, he finished his summer research with Albert-Ludwigs-Universitt Freiburg, Germany, studying mechanical transducer modeling and simulation.

Mr. Xu received the E. C. Jordan Award in 2013, the Russell E. Berthold Scholarship in 2012, and the Floyd E. Lundgren Scholarship in 2012 for undergraduate students with the Department of Electrical Computer Engineering. He was also a member of the University of Illinois Solar Decathlon Team.

Lei Jin (S'10) was born in Changzhou, China, in 1988. He studied mechanical engineering at Beihang University, Beijing, China, from 2007 to 2010. He received the B.S. degree in electrical engineering from the University of Illinois at Urbana-Champaign (UIUC), Urbana, IL, USA, in 2013.

He has been a Teaching Assistant for microelectronic circuits with UIUC since 2012. His current research interest includes power electronics, photovoltaics, and circuit design.

Mr. Jin is a James Scholar at UIUC. He received the Henry O. Koehler Scholarship in 2011 and the International Engineering Fellowship in 2012.

Philip T. Krein (S'76–M'82–SM'93–F'00) received the B.S. degree in electrical engineering and the A.B. degree in economics and business from Lafayette College, Easton, PA, USA, and the M.S. and Ph.D. degrees in electrical engineering from the University of Illinois, Urbana-Champaign, IL, USA.

He was an Engineer with Tektronix, Beaverton, OR, USA. He then returned to the University of Illinois at Urbana-Champaign. He currently holds the Grainger Endowed Director's Chair in Electric Machinery and Electromechanics as a Professor and the Director of the Grainger Center for Electric Machinery and Electromechanics, Department of Electrical and Computer Engineering. He has published an undergraduate textbook entitled *Elements of Power Electronics* (Oxford, U.K.: Oxford Univ. Press, 1998). In 2001, he helped initiate the IEEE International Future Energy Challenge, which is a major student competition involving fuel cell power conversion and energy efficiency. He holds 25 U.S. patents with additional patents pending. His research interests include all the aspects of power electronics, machines, drives, and electrical energy, with emphasis on nonlinear control and distributed systems.

Dr. Krein is a Registered Professional Engineer in both Illinois and Oregon. He was a Senior Fulbright Scholar with the University of Surrey, Surrey, U.K., and was recognized as a University Scholar, which is the highest research award at the University of Illinois. In 2003, he received the IEEE William E. Newell Award in Power Electronics. He is a Past President of the IEEE Power Electronics Society (PELS) and served as a member of the IEEE Board of Directors. In 2005–2007, he was a Distinguished Lecturer for the IEEE PELS, and in 2008, he received the PELS Distinguished Service Award. He is an Associate Editor of the IEEE TRANSACTIONS ON POWER ELECTRONICS and serves as Academic Advisor for the Department of Electronic and Information Engineering with Hong Kong Polytechnic University. He is a Founder and Director of SolarBridge Technologies: a developer of long-life integrated solar energy systems.